Photonic crystal based radiochromic dosimeter for electron-beam irradiation with superior spatial and dose resolution

Zhihao Wang[1], Jun Ma[1,2]*

[1]College of Materials Science and Technology, Nanjing University of Aeronautics and Astronautics, Nanjing 211106, China
[2]School of Nuclear Science and Technology, University of Science and Technology of China, Hefei 230026, China
*Corresponding author.
Emails: majun0502@ustc.edu.cn

Abstract
Electron-beam (e-beam) technology display widespread applications that heavily relies on the delivered dose and irradiated geometrical area. However, the immediate visualization of precise e-beam dose and spatial dose distribution is challenging due to high throughput flux and strong electron scattering. Herein, we developed wide dose-response range (0–3750 kGy) and high spatial resolution (<100 μm) e-beam dosimetry based on photonic crystal polymer films. Notably, the diffraction peak of the inverse opal film exhibits a continuous blue shift with increased dose within the visible light wavelength range. The naked-eye readable dosimeter showed excellent pre- and post-irradiation stability, which means it is resistance to environmental factors such as temperature and ultraviolet exposure. We suggested that these advantages make photonic crystal films promising candidates for high-dose e-beam dosimetry and beam uniformity evaluation.

Keywords: electron beam; photonic crystal; radiochromic film; high dose detection; high spatial resolution

1 Introduction
Electron beam (e-beam) technology has been appreciated by a wide range of applications in public health, agriculture, medicine, the environment, and the materials industry,[1-3] because it displays significant advantages such as minimal ecological impact, operational simplicity, and scalability.[4-17] In addition, e-beam is also a powerful tool to synthesis advanced functional materials that is inaccessible by conventional thermal or chemical methods. For instance, e-beam technology enables the efficient synthesis of zeolite molecular sieves under ambient conditions and facilitates the one-step, in-situ production of gel-electrolyte lithium batteries and capacitors.[18-20] The accurate detection of dose and the uniformity of e-beam distribution is the key points in controlling the process. Regions receiving insufficient doses may not achieve the desired physical or chemical modifications, whereas over-exposed areas may suffer from material damage or thermal degradation due to localized energy concentration. However, the naked-eye read of absorbed dose and spatial dose distribution is challenging due to high throughput flux and strong electron scattering.
Thin-film dosimeters, characterized by their tunable dose range and high spatial resolution,

present a promising approach for mapping two-dimensional electron beam dose distributions. Currently, the GEX B3 WINdose and FWT-60 films are the predominant commercially available options for high-dose electron beam (e-beam) detection. These dosimeters are widely used due to the broad detection range, stable response, ease of measurement, and cost-effectiveness. Nonetheless, these thin films are made by radiation-sensitive dye materials, thus the dosimeter stability is markedly influenced by environmental factors such as temperature, humidity, static electricity, ultraviolet radiation, and oxygen exposure. Moreover, these films suffer from post-irradiation effects, and necessitate heat treatment to stabilize their response, which in turn, imposes limitations on beam detection accuracy and effectiveness. Thus far, few radiations dosimeter that can combines a high e-beam dose detection range, excellent environmental stability, and naked-eye readings, which is necessary in practical use.

Photonic crystals, based on structural color from the interaction of light with periodic nanostructures, have garnered significant attentions for their diverse applications in stimuli-responsive sensors, photon printing, and information storage.[21-28] Recently, we observed that the diffraction peak of photonic crystal (PC) films exhibits a blue shift under γ/X-ray irradiation as the absorbed dose increases, accompanied by a corresponding change in color.[29, 30] However, the dose-response behavior and underlying mechanisms of photonic crystal films under ultra-high dose rate electron beam irradiation remain poorly understood and warrant further investigation.

In present work, we address the challenging by using an electron accelerator to assess photonic crystal film dosimetric properties. The radiation response characteristics of photonic crystal polymer films under e-beam irradiation was comprehensively investigated, Systematic characterization reveals a distinct blue shift in the diffraction peak accompanied by a visible color transition from red to blue with increasing absorbed dose. Therefore, we propose a viable photonic crystal-based e-beam dosimeter through a precise calibration curve between absorbed dose and diffraction peak displacement. The dosimeter has an extensive dose response range (0-3750 kGy) and exceptional spatial resolution (<100 μm). Notably, the dosimeter exhibits outstanding stability under various conditions. Pre-irradiation stability tests show no color change after 6 hours of thermal aging at 70°C or exposure to 36 W UV irradiation. Post-irradiation analysis confirms the stability of diffraction spectra and radiation response for at least 38 days. This dosimeter combines several advantageous features: a broad dose detection range, superior spatial resolution, excellent pre- and post-irradiation stability, straightforward operation, and naked eye readout capability. These comprehensive characteristics position the inverse opal films as highly promising candidates for advanced radiation detection applications, particularly in high-dose e-beam dosimetry and e-beam uniformity assessment.

2 Results and Discussions

2.1 Fabrication of PEGDA PC films

The fabrication process of a typical photonic crystal inverse opal film is illustrated in Figure S1A, with additional details provided in the Experimental Section. A highly ordered silica colloidal crystal template (Figure S1B) was employed to prepare an inverse opal film exhibiting a bright red color, corresponding to a diffraction peak at ~659 nm, as shown in Figure S1D. Briefly, silica particles (~335 nm) dispersed in ethanol were drop-cast onto a flat glass slide (5 cm × 7 cm). A colloidal crystal array formed via the self-assembly of silica microspheres during ethanol evaporation. Subsequently, a polyethylene glycol diacrylate (PEGDA) polymer precursor solution containing a UV photoinitiator (2,2-dimethoxyacetophenone) was infiltrated into the voids of the

silica array. The precursor solution was then cured under UV irradiation, resulting in a polymer composite film embedded with silica crystals. Finally, the silica template was etched away using a 2% hydrofluoric acid (HF) aqueous solution, followed by triple cleaning to yield an inverse opal PEGDA film with a well-defined porous structure (Figure S1C).

Due to the orderly packing of the silica colloidal crystal templates, light propagating at certain wavelengths was prevented in the inverse opal films, forming the brilliant structural colors with a characteristic diffraction peak at 659 nm (Figure. S1D). The peak can be expressed according to the Bragg-Snell equation as follows:[24]

$$\lambda_{max} = 1.633 \frac{d}{m} \sqrt{\sum n_i^2 V_i - \sin^2 \theta} \tag{1}$$

where λ_{max} is the wavelength of the Bragg diffraction peak; d is the characteristic length of the periodical structure in the PCs; m is the order of the Bragg diffraction; n_i and V_i are the effective refractive index and the volume fraction of the material, and θ is the angle measured from normal incidence. Both characteristic length (d), and refractive index (n) can be altered to change the PGB wavelength of PC films. Upon electron beam irradiation, the refractive index of the photonic crystal (PC) film remains largely unchanged; however, radiation-induced crosslinking or scission of the crosslinked polymer chains can result in microstructural change. This disruption alters the periodic spacing of the assembly, leading to a shift in the diffraction peak wavelength (λ_{max}) that correlates with the absorbed dose.

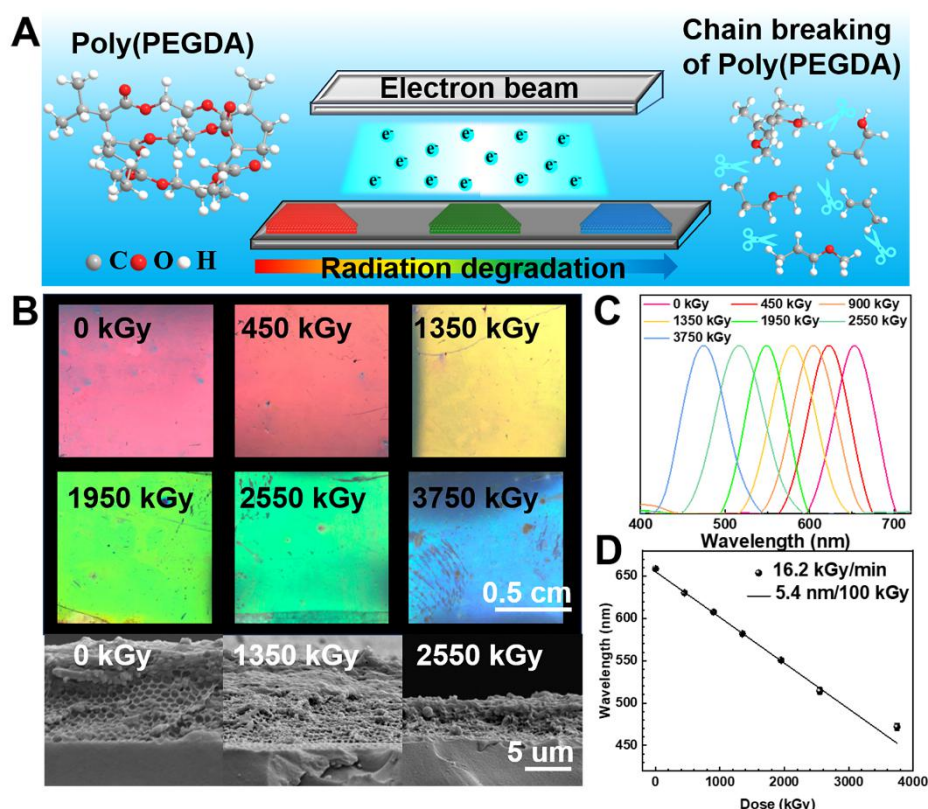**2.2 Dosimetry of PC thin films under electron beam**

Figure 1. Fabrication and radiochromic properties of inverse opal dosimeter. (A) Schematic diagram of electron beam irradiation and discoloration of the inverse opal PEGDA PCs; (B) The digital images of PEGDA PC films changes with absorbed dose and SEM images of their corresponding cross-section morphology; (C) spectra and Bragg diffraction peak wavelengths of inverse opal films after

being irradiated with doses from 0 to 3750 kGy; (D) The Bragg diffraction peaks of the vary linearly with the absorbed dose in the range of 0 kGy to 3750 kGy.

The red inverse opal film was irradiated using an electron accelerator at a dose rate of 16.2 kGy/min to assess its dosimetric properties, as illustrated in Figure 1A. With absorbed dose increasing, the film's color transitioned gradually from red to blue. Cross-sectional scanning electron microscopy (SEM) imaging revealed structural changes in the inverse opal architecture during irradiation. Prior to irradiation, the inverse opal PEGDA membrane displayed a well-ordered, multilayered porous structure. However, as the absorbed dose increased (0–3750 kGy), the periodic pore structure progressively collapsed, as shown in Figure 1B. Concurrently, the diffraction spectrum exhibited a continuous blue shift, with the peak decreasing from 659 nm at 0 kGy to 471 nm at 3750 kGy (Figure 1C), consistent with predictions derived from the Bragg diffraction equation. By fitting the relationship between the diffraction peak position and absorbed dose, a strong linear correlation was established, confirming that the film's color change can serve as a reliable and quantitative indicator of radiation dose. The film demonstrated a sensitivity of 5.4 nm/100 kGy, highlighting its potential as a high-performance dosimeter for high-dose electron beam applications (Figure 1D). These findings underscore the utility of photonic crystal films as a robust and visually interpretable platform for advanced radiation dosimetry.

In our previous investigation, we examined the radiation response characteristics of inverse opal films to γ-ray irradiation in atmospheric conditions.[30] The study revealed a response sensitivity of 83 nm/100 kGy when exposed to gamma rays at a dose rate of 15.7 Gy/min, demonstrating substantially higher sensitivity compared to the 5.4 nm/Gy observed under oxygen-free electron beam irradiation. The dose required for the complete collapse of the inverse opal structure of the photonic crystal polymer film under electron beam irradiation is much higher than that required by gamma ray irradiation. The reason may be related to the high dose rate effect of electron beam irradiation and the absence of oxygen in the process of electron beam irradiation. The relationship between polymer molecular weight(M_c) and absorbed dose during electron beam irradiation can be expressed by formula 2.[31]

$$\frac{1}{M_c} = \frac{1}{M_{c,0}} + k_1(4G(x) - G(s))D \qquad (2)$$

Where G(s) is the radiation chemical yield of chain break (the free base generated when absorbing 100 eV), G(x) is the radiation chemical yield of intermolecular crosslinking, and D is the absorbed dose.

As indicated by Equation 2, the molecular weight (Mc) of PEGDA decreases with absorbed dose increasing, and this process is strongly influenced by both the chain crosslinking yield G(x), and the chain scission yield G(s). It has been reported that the G(s) and G(x) of PEGDA in the atmospheric environment are 24.9 and 3.6, respectively, suggesting that chain scission predominates under these conditions. However, under N_2 conditions, G(s) decreases to 6.4, while G(x) decreases to 1.0, indicating a decreasing of both chain crosslinking and chain degradation.[31] This contrast highlights that, compared to γ-irradiation in air, the degradation rate of PEGDA is reduced during electron beam irradiation in N_2. The primary cause of this difference lies in the presence of oxygen in the atmospheric environment, which reacts with free radicals to form peroxy free radicals, thereby accelerating the polymer degradation process. In contrast, the absence of oxygen in the N_2 environment significantly slows down the degradation rate. At the same time, the radiation-induced crosslinking of polymer chains in N_2 further mitigates the

degradation process, contributing to a decrease in the overall rate of radiative degradation. These findings underscore the critical role of the gaseous environment in modulating the radiation effects on polymers, with oxygen presence or absence influencing both the crosslinking and degradation behaviors during radiation irradiation. Moreover, the electron accelerator has a higher radiation dose rate than ^{60}Co gamma radiation source, and the higher dose rate leads to an increase in the probability of free radical recombination, which may also be one of the reasons for the decrease in radiation sensitivity.

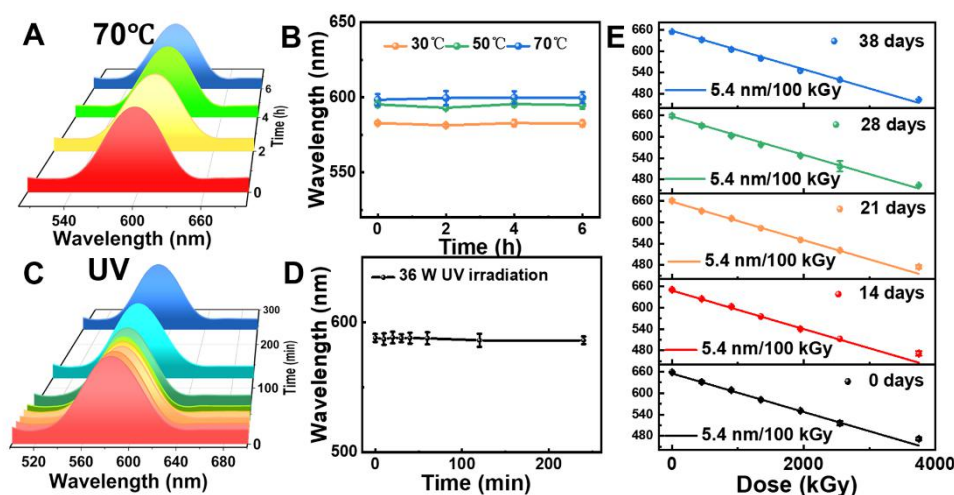**2.3 Pre-irradiation and post-irradiation stability of PEGDA PC films**

Figure 2. Pre-radiation and post-radiation stability of inverse opal films. The spectra (A) and the Bragg diffraction peaks (B) of unirradiated inverse opal film stored in a 70 ℃ oven for various times; The spectra (C) and the Bragg diffraction peaks (D) of unirradiated inverse opal film with 36W UV-irradiation for various times; (E) The Bragg diffraction peaks of the films storing for different time vary linearly with the absorbed dose in the range of 0 kGy to 3750 kGy.

Temperature and ultraviolet (UV) exposure are critical environmental factors that can significantly compromise the performance of traditional radiochromic dosimeters during storage. Elevated temperatures and UV radiation often induce polymerization or degradation of dye molecules, leading to dosimeter failure. In contrast, photonic crystals, characterized by their periodic nanostructures and photonic band gaps, exhibit structural colors that remain stable over time without fading, offering exceptional environmental stability. This inherent stability enables photonic crystal-based dosimeters to overcome the limitations of traditional dye-based systems. To evaluate the thermal stability of the photonic crystal films, samples were stored at 30°C, 50°C, and 70°C for 6 hours, the diffraction spectra of the films were measured at 0, 2, 4, 6h, as shown in Figures 2A and 2B. No significant shift in the diffraction peaks was observed over time, and the films maintained their structural color, demonstrating robust thermal stability. Additionally, the films were subjected to 6 hours of UV irradiation using a 36 W UV lamp to assess their resistance to low-energy UV exposure. The diffraction spectra of the films were measured at 0, 10, 20, 30, 40, 60, 120 and 240min, as shown in Figures 2C and 2D. The diffraction spectra maintained unchanged, confirming excellent UV stability. These experiments collectively demonstrate that the films can maintain their pre-irradiation stability, and unaffected by moderate temperature fluctuations and low-energy UV exposure.

The post-irradiation stability of the dosimeter is equally critical, as traditional dye-based radiochromic films often exhibit distortion of radiation information during prolonged storage. To evaluate the post-irradiation stability of the photonic crystal thin film dosimeter, diffraction spectra were recorded at 0, 14, 21, 28, and 38 days after irradiation (Figures 2E, S2, and S3). The spectra revealed no significant deviations in diffraction peaks compared to the initial measurements taken immediately after irradiation, indicating that the photonic crystal films can reliably store electron beam dose information over extended periods. Furthermore, the dosimeter's sensitivity remained consistent with prolonged storage, underscoring its excellent post-irradiation stability and reliability for long-term dose recording. These findings highlight the exceptional stability of photonic crystal films, both before and after irradiation, making them highly suitable for accurate and long-term radiation dose measurement. Their resistance to environmental factors and ability to maintain dose information position them as a promising alternative to traditional dosimeters in applications requiring reliable and durable radiation detection.

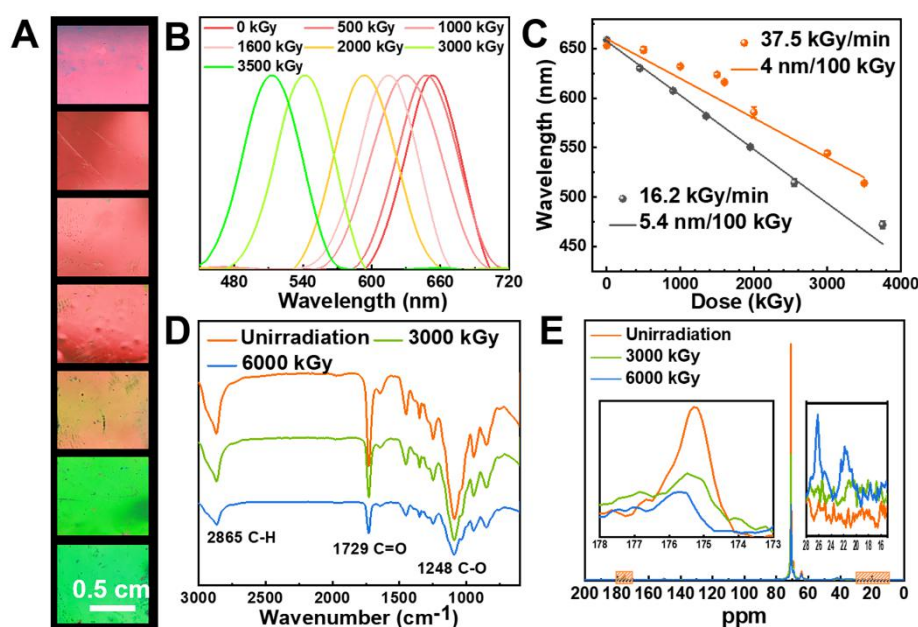## 2.4 Effect of dose rate and degradation principle

Figure 3. Radiochromic dosimeter of inverse opal film with dose rate of 37.5kGy/min. (A) Digital photographs of inverse opal PEGDA films irradiated with gradient absorbed doses; (B) Spectra shift of inverse opal PEGDA films irradiated with gradient absorbed doses; (C) Bragg diffraction peak wavelengths of inverse opal films with dose rate of 37.5 kGy/min and 16.2 kGy/min after being irradiated with gradient absorbed doses; FTIR(D) and 13C NMR(E) of inverse opal PEGDA films irradiated with different doses.

As previously discussed, the radiation effects on polymers are strongly influenced by dose rate, highlighting the importance of evaluating the dose-rate sensitivity of radiochromic photonic crystal films. To investigate this, the films were irradiated using an electron beam at an elevated dose rate of 37.5 kGy/min. As the absorbed dose increased, the color of the film transitioned visibly from red to green, accompanied by a continuous blue shift in the diffraction peak of the photonic crystal structure, with the peak wavelength decreasing from 653 nm at 0 kGy to 513 nm at 3500 kGy, consistent with predictions derived from the Bragg diffraction equation (Figures 3A and 3B). The radiation sensitivity of the photonic crystal films at the higher dose rate was

determined to be 4 nm/100 kGy, which is lower than the sensitivity of 5.4 nm/100 kGy observed at a lower dose rate of 16.2 kGy/min (Figure 3C).

This reduction in sensitivity at higher dose rates is attributed to the increased concentration of free radicals generated during electron beam irradiation. The higher concentration of free radicals enhances the probability of radical recombination following polymer chain scission, thereby reducing the extent of radiation-induced damage to the polymer network at the same absorbed dose. This phenomenon results in a decrease in the overall radiation sensitivity of the photonic crystal thin film dosimeter at higher dose rates. These findings provide critical insights into the dose-rate dependence of photonic crystal films, underscoring their potential for tunable applications in high-dose radiation environments. However, they also emphasize the necessity for careful calibration under varying irradiation conditions to ensure accurate and reliable dosimetry. This understanding is essential for optimizing the performance of photonic crystal-based dosimeters in diverse radiation processing applications.

As mentioned earlier, the presence of oxygen plays a pivotal role in modulating radiation-induced cross-linking and chain scission processes in polymers. Under ambient conditions, ionization triggers the rapid reaction of polymer-generated free radicals with oxygen, forming peroxy radicals that accelerate degradation. In contrast, when irradiation is performed under nitrogen or vacuum, the absence of oxygen significantly reduces radiation-induced chain scission, thereby decelerating polymer degradation. In such oxygen-deprived environments, both cross-linking and scission reactions occur along the polymer backbone, albeit at a much slower rate compared to air. Under electron beam irradiation, the main chain of poly(PEGDA) (CH_2–CH_2–O–) undergoes scission, yielding free radicals that subsequently recombine or undergo disproportionation, resulting in various radiation-induced products. Detailed reaction mechanisms are outlined in the Supplementary Information.[32]

To investigate the chemical transformations in photonic crystal films induced by electron beam irradiation, we conducted infrared (IR) spectroscopy and solid-state nuclear magnetic resonance (NMR) analyses of inverse opal films irradiated at different doses (Figures 3D, 3E, and Supplementary Figures S3). The IR spectra (Figure 3D) reveal dose-dependent changes in vibrational modes characteristic of PEGDA. The C–H stretching and bending vibrations at 2865 cm^{-1} and 1450 cm^{-1}, respectively, show a notable decrease in transmittance with increasing dose, consistent with C–H bond cleavage initiated by free radicals. Similarly, the C=O stretching vibration at 1729 cm^{-1} diminishes, indicating cleavage of carbonyl bonds during irradiation. Moreover, the C–O–C stretching vibrations at 1248 cm^{-1} and 1091 cm^{-1} weaken, corroborating the breakage of ether linkages.[32-38] Solid-state ^{13}C NMR spectra (Figure 3E) further substantiate these findings, highlighting structural alterations in the polymer matrix. The peak at 175 ppm, corresponding to the C=O group, decreases in intensity with rising radiation dose, mirroring the IR results. Simultaneously, the peak at 70 ppm, linked to the –CH_2– backbone, diminishes, while peaks at 20–30 ppm intensify, indicating cleavage of the polymer's main chain and the formation of shorter chains under irradiation.[39]

Integrating insights from radical reaction pathways, IR spectroscopy, and NMR analyses, it is evident that PEGDA inverse opal films primarily undergo radiation-induced degradation under high-dose electron beam exposure, despite the coexistence of cross-linking reactions. Additionally, literature reports suggest that high-dose irradiation not only facilitates chemical bond cleavage and reorganization but also generates gaseous by-products such as H_2, CO, CO_2, and organic

volatiles.[40, 41] The evolution of these gases provides further evidence of polymer degradation under high-dose irradiation. This degradation drives the progressive collapse of the photonic crystal's porous structure, which manifests as a pronounced blue shift in the diffraction spectrum. At the macroscopic level, this structural collapse results in a visible color transition of the film, shifting from red to green. These findings elucidate the key mechanisms governing the optical and structural transformations in PEGDA films subjected to high-dose electron beam irradiation, providing a comprehensive understanding of their radiation response behavior.
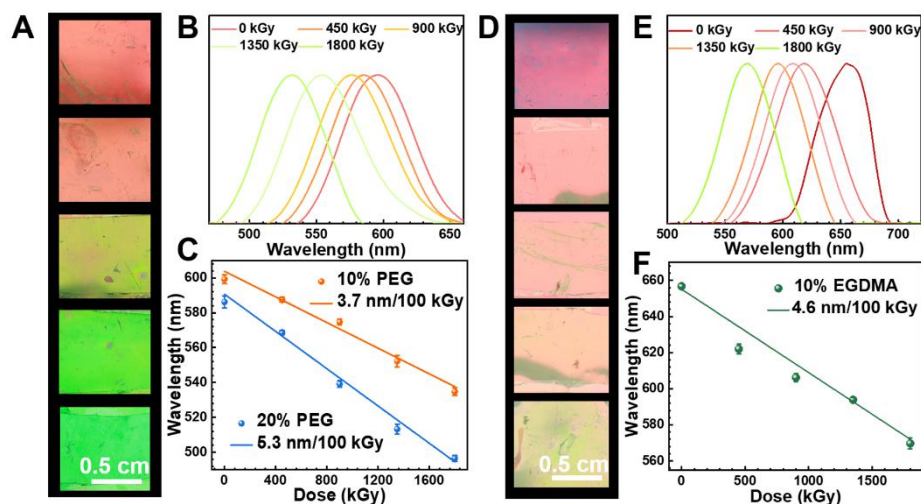
2.5 Adjustment of sensitivity

Figure 4. Effect of crosslinking density. (A) Digital photographs of PEG plasticized (10%) inverse opal PEGDA films irradiated with gradient absorbed doses; (B) Spectra shift of PEG plasticized (10%) inverse opal PEGDA films irradiated with gradient absorbed doses; (C) Bragg diffraction peak wavelengths of PEG plasticized(10% and 20%) inverse opal films after being irradiated with gradient absorbed doses; (D) Digital photographs of inverse opal PEGDA films(soaked in 10% EGDMA solution) irradiated with gradient absorbed doses; (E) Spectra shift of inverse opal films(soaked in 10% EGDMA solution) irradiated with gradient absorbed doses; (F) Bragg diffraction peak wavelengths of inverse opal PEGDA films(soaked in 10% EGDMA solution) irradiated with gradient absorbed doses.

Previous studies have demonstrated that during γ-irradiation of polymer films in air, the incorporation of polyethylene glycol (PEG)—a polymer devoid of double bonds—into the polymer precursor solution effectively reduces the crosslinking density of the polymer network. This reduction enhances radiation-induced degradation, thereby increasing the sensitivity of photonic crystal dosimeters[30]. To explore the modulation mechanism of electron beam radiation sensitivity in photonic crystal films, we irradiated films containing varying percentages of PEG using an electron accelerator. The results are presented in Figure 4A and Supplementary Figure S4. The inclusion of PEG reduced the crosslinking density of the polymer films, leading to a decrease in the initial diffraction peak wavelength of the photonic crystal films. When the doping amount of PEG is 0%, the diffraction peak of the film is observed at 659 nm. Upon increasing the PEG doping to 10%, the diffraction spectrum exhibits a significant blue shift, with the peak position decreasing to 599 nm. Further increasing the PEG doping to 20% results in a smaller blue shift, with the diffraction peak position slightly decreasing to 586 nm. With the increase of absorbed dose, the color of the films with different PEG doping amount showed a continuous blue shift. When PEG doping is 10%, the diffraction peak wavelength decreases from 599 nm at 0kGy to 534

nm at 1800kGy; when PEG doping is 20%, the diffraction peak wavelength decreases from 586nm at 0kGy to 496nm at 1800kGy (Figure 4A-C). However, in contrast to γ-irradiation in air, the addition of PEG reduced the radiation sensitivity of the films under a nitrogen atmosphere. For instance, films with 10% PEG exhibited a sensitivity of 3.7 nm/100 kGy, while those with 20% PEG demonstrated a sensitivity of 5.3 nm/100 kGy, both lower than the 5.4 nm/100 kGy observed in pure PEGDA films. This reduction in sensitivity is attributed to radiation-induced crosslinking reactions occurring in the absence of oxygen. At low PEG concentrations (10%), crosslinking between PEG and PEGDA during irradiation mitigates damage to the microscopic photonic crystal structure caused by radiation-induced degradation. At higher PEG concentrations (20%), the porous structure of the photonic crystal is primarily maintained by the crosslinked PEGDA network. Although increased PEG-PEGDA crosslinking occurs during irradiation, the supporting PEGDA network becomes compromised, resulting in higher sensitivity compared to films with lower PEG content. These findings suggest that the concentration of PEG plays a critical role in modulating the sensitivity and structural response of photonic crystal films to high-dose electron beam irradiation, offering insights into the design of tunable dosimeters for advanced applications.

To further investigate the influence of crosslinking agents, ethanol solutions with varying proportions of ethylene glycol dimethacrylate (EGDMA) were prepared. The anti-opal films were immersed in EGDMA-ethanol solutions, allowing the polymer network and porous photonic crystal structure to be thoroughly infiltrated by the mixture. The films were subsequently subjected to electron beam irradiation across varying dose gradients. The irradiated films were then analyzed to assess the effect of EGDMA content on radiation response, as shown in Figure 4D, 4E, and Supplementary Figures S5 and S6.

When the volume fraction of EGDMA was 10%, the film's color shifted to yellow with increasing radiation dose, accompanied by a gradual blue shift in the diffraction peak (Figure 4D, 4E). As the absorbed dose increased, the film color transitioned visibly from red to yellow, accompanied by a continuous blue shift in the diffraction peak of the photonic crystal structure, with the peak wavelength decreasing from 657 nm at 0 kGy to 570 nm at 1800 kGy, consistent with predictions derived from the Bragg diffraction equation (Figures 4D-E). These films exhibited a radiation sensitivity of approximately 4.6 nm/100 kGy, lower than the 5.4 nm/100 kGy of pure PEGDA films. However, with higher EGDMA contents (50% or 100%), the diffraction spectra showed minimal changes across varying irradiation doses (Supplementary Figures S5 and S6). Scanning electron microscopy (SEM) of films immersed in 50% EGDMA revealed that the porous structure remained largely intact, even at high radiation doses. The addition of EGDMA increased the crosslinking density of the polymer, stabilizing the photonic crystal structure and significantly reducing the effect of radiation on diffraction peaks and color. These findings suggest that incorporating EGDMA enhances structural integrity under high-dose electron beam irradiation, offering a promising strategy for tuning the performance of photonic crystal dosimeters.
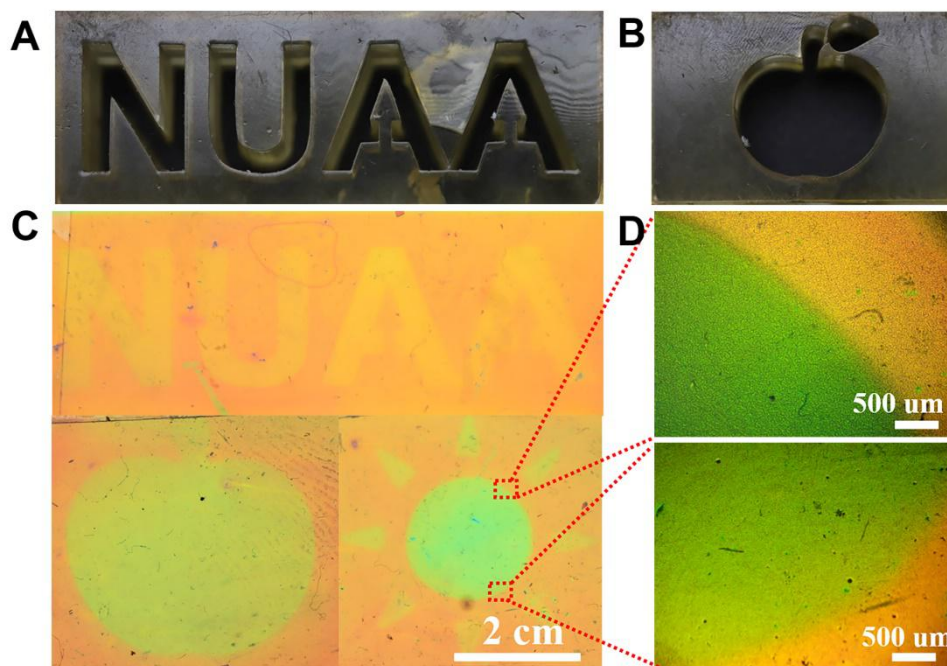
2.6 Patterning and resolution

Figure 5. Patterning and resolution of inverse opal film. (A) And (B) Digital photos of 3D printing mask; (C) Digital photo of PEGDA inverse opal films irradiated in the patterned radiation field; (D) Enlarged area of microscopic images of C (scale bars 500 μm).

The spatial resolution of thin-film dosimeters is a critical parameter for evaluating their performance, particularly in assessing beam uniformity in electron accelerators and characterizing beam distribution in large-scale scientific platforms such as synchrotron radiation facilities. When an electron beam interacts with a metal, scattering occurs due to interactions between the incident electrons and the electrons within the metal, leading to a decrease in beam density. This scattering degrades image quality and machining precision. Conversely, non-metallic insulating materials exhibit weaker scattering effects, allowing the electron beam to maintain higher density, resulting in improved imaging and processing fidelity.

To evaluate the spatial resolution of inverse opal films for electron beam scattering, experiments were conducted using polyurethane and metal masks, as illustrated in Figure 5 and Figures S8 and S9. Polyurethane templates with various patterns were fabricated using digital light processing (DLP) 3D printing, as shown in Figure 5A and 5B. These hollow templates served as selective shielding, blocking portions of the electron beam to create specific radiation field distributions. After irradiation, distinct discoloration patterns corresponding to designs such as NUAA, an apple, and a sun were observed on the photonic crystal films (Figure 5C). Optical microscopy of the irradiated solar pattern revealed a sharp transition boundary of less than 100 μm between irradiated and unirradiated regions. Corresponding diffraction spectra for these regions are provided in Figure S8. There are obvious spectral differences between the irradiated region and the irradiated region. The diffraction peak in the unirradiated region is 578nm, while the diffraction peak in the irradiated region is reduced to 527nm. In contrast, when a metal template was used to shield the electron beam, visible scattering effects caused by the metal were evident. A broad yellow transition boundary, exceeding 500 μm, was observed via optical microscopy (Figure S9A and S9C). Spectrometer analysis further confirmed distinct diffraction spectra for the irradiated, unirradiated, and transition regions (Figure S9B). The unirradiated region exhibited a

diffraction peak at 638 nm, while the irradiated region showed a peak at 517 nm. The transition region displayed an intermediate peak position of 569 nm. These results underscore the superior spatial resolution of the photonic crystal colorimetric films, capable of resolving and quantifying electron beam scattering fields with high precision. This exceptional spatial resolution makes the photonic crystal film dosimeter a powerful tool for high-accuracy beam uniformity and distribution measurements, demonstrating its utility for advanced applications in electron beam diagnostics and precision machining.

3 Conclusion

In summary, we present a photonic crystal-based photochromic film as an innovative dosimeter for high-dose electron beam radiation, uniquely capable of simultaneously detecting radiation dose levels and beam distribution uniformity. A precise correlation between the diffraction peak shift and absorbed dose was established, demonstrating a dynamic response range from 0 to 3750 kGy, with a sensitivity of 5.4 nm/100 kGy. The mechanism underlying the discoloration of PEGDA photonic crystal films under high-dose electron irradiation in a nitrogen atmosphere was systematically investigated, revealing insights into the structural and chemical transformations. The inclusion of PEG and EGDMA enabled modulation of the dosimeter's response range and sensitivity, providing tunable properties to suit diverse applications. Notably, the photonic crystal film exhibited remarkable stability both before and after irradiation. Pre-irradiation tests confirmed that the film could withstand preservation at 70°C and exposure to 36 W UV radiation for at least 6 hours without diffraction peak blue shift. Post-irradiation assessments demonstrated that the diffraction peak shift and dose sensitivity remained stable for up to 38 days following exposure. Furthermore, the dosimeter achieved exceptional spatial resolution, finer than 100 μm, enabling precise assessment of beam distribution uniformity. Compared to conventional dosimeters, this photonic crystal-based system offers a unique combination of high-dose response capability, outstanding pre- and post-irradiation stability, and superior spatial resolution. These features highlight its significant potential for advanced applications in high-dose electron beam radiation detection and radiation field uniformity analysis.

4 Material and methods

4.1 Materials.

Tetraethyl orthosilicate (AR) (TEOS), polyethylene glycol (AR) (PEG, Mn=600) and polyethylene glycol diacrylate (AR) (PEGDA, Mn=400) were purchased from Macklin Biochemical Co., Ltd (Shanghai, China). Ammonium hydroxide, ethanol, and Hydrofluoric acid (HF) were purchased from Nanjing Chemical Reagent Co., Ltd (Nanjing, China). 2,2-diethoxyacetophenone (DEAP) (95.0%, GC) and Ethylene glycol dimethacrylate (EGDMA) was purchased from Aladdin Biochemical Technology Co., Ltd (Shanghai, China). Ultrapure water was used in all experiments.

4.2 Preparation of Inverse Opal PEGDA films, PEGDA/PEG films and EGDMA fills PEGDA films.

Monodisperse silica microspheres of varying particle sizes were synthesized via the classical Stöber method. Following the reaction, the silica microspheres were subjected to sequential cleaning cycles involving centrifugation and re-dispersion (at least three repetitions) in water and ethanol, effectively removing unreacted ammonia and tetraethyl orthosilicate. The purified silica microspheres were then dispersed in ethanol for subsequent use. Using an optimized dip-coating

method, these microspheres were self-assembled into highly ordered colloidal crystal templates on a glass substrate.

A polymer precursor solution, composed of polyethylene glycol diacrylate (PEGDA-400, 99% (v/v)) and a photoinitiator (DEAP, 1% (v/v)), was infiltrated into the interstitial gaps of the silica microsphere arrays via capillary action. This assembly was then covered with a second glass sheet, separated by a polytetrafluoroethylene spacer. The monomer solution was polymerized under irradiation with a 36 W UV lamp for 20 minutes, yielding a cured polymer film with precise thickness controlled by the spacer dimensions. The resulting PEGDA composite film, embedded with a silica colloidal array, was peeled off and immersed in 5.0% (v/v) HF solution for 2 hours to etch away the silica template. Following thorough washing and drying, a bright PEGDA film with structural color was obtained.

PEGDA in the precursor solution was replaced by PEGDA-400/PEG-600 mixed solution, and the PEG/PEGDA ratio was 10% and 20%, respectively. The above preparation process was repeated to obtain the inverse opal PEGDA/PEG membrane. After the etching is complete, the PEGDA/PEG photonic crystal film is soaked in ethanol and dried to form a film with a bright structural color.

EGDMA was mixed with ethanol, and ethanol solutions with different EGDMA volume fractions were configured. After the inverse opal film is immersed in ethanol solution with different volume fraction of EGDMA, the EGDMA is completely immersed in the polymer network and porous structure of the anti-opal film, and the EGDMA filled PEGDA photonic crystal film is obtained.

4.3 Radiation Responses of Inverse Opal Films.

Inverse opal PEGDA (Mn=400) films were irradiated using an electron accelerator at dose rates of 16.2 kGy/min and 37.5 kGy/min, respectively, with the photonic crystal structured surface facing upward to receive direct electron beam irradiation. The influence of varying absorbed doses on the films was systematically investigated. Additionally, PEGDA/PEG films containing 10% and 20% PEG were subjected to electron beam irradiation at a dose rate of 16.2 kGy/min to evaluate the effect of PEG incorporation on the radiation response. To study the role of glycol dimethacrylate (EGDMA), PEGDA films were immersed in ethanol solutions with varying EGDMA volume fractions and subsequently irradiated at a dose rate of 16.2 kGy/min. The impact of EGDMA on the radiation sensitivity of the films was analyzed. Additionally, the spatial resolution of the anti-opal film dosimeters was evaluated using metal and polyurethane stencils to selectively shield the electron beam, generating radiation fields with well-defined patterns. This approach allowed for a detailed assessment of the films' ability to resolve and measure complex radiation field distributions.

4.4 Pre-irradiation and post-irradiation stability of Inverse Opal Films.

Pre-irradiation stability: The prepared PEGDA (400) photonic crystal film was stored in different temperature fields, and the temperature stability of the film was evaluated by measuring the change of diffraction spectrum with time. PEGDA (400) photonic crystal films were irradiated with a 36 W UV lamp, and the UV resistance of the films was evaluated by measuring the change of diffraction spectra over time.

Post-irradiation stability: By measuring the diffraction spectra of films with different doses of radiation and stored for different times, the change of spectra with time was studied, and then the post-radiation stability of the films was evaluated.

4.5 Devices and Measurements.

PEGDA was UV-cured using a 365 nm UV lamp (36 W). The morphology of the inverse opal film was characterized by scanning electron microscopy (SEM) using a Hitachi SU8220 field emission scanning electron microscope (Japan). ^{13}C-NMR analysis was performed on a Bruker AVANCE NEO 400M spectrometer (Germany). Fourier transform infrared (FTIR) spectroscopy was conducted with a Thermo Fisher Scientific Nicolet iS5 instrument (USA). Photographs and videos were captured using a Nikon D3100 digital camera. Reflectance spectra of the inverse opal film were recorded with a Seeman S2000-VIS spectrometer (330nm-1100nm, Hangzhou Siman Technology). Radiation experiments on the inverse opal films were carried out at Jiangsu Zhiyan Technology Co., Ltd. and Hubei Xiangyuan New Material Technology Co., Ltd. The different shapes of polyurethane hollow patterns were prepared by DLP light curing 3D printer (Photon Mono 2, Shenzhen Anycubic Technology Co., LTD.).

Author contributions. All authors contributed to the study conception and design. Material preparation, data collection and analysis were performed by Zhi-hao Wang. Jun Ma commented and optimized the manuscript. All authors read and approved the final manuscript.

Data availability. The data supporting this article have been included as part of the Supplementary Information.

Declarations

Conflicts of interest. The authors declare that they have no Conflict of interest.

Reference

1. A. Šagátová, M. Fülöp, M. Pavlovič et al., Electron-Beam Accelerator with Conversion to X-Rays: Optimal Radiation Type According to Application. Radiat. Phys. Chem. **172**, (2020). http://doi.org/10.1016/j.radphyschem.2020.108789

2. R. Andok, A. Bencurova, K. Vutova et al., Study of the New Csar62 Positive Tone Electron-Beam Resist at 40 Kev Electron Energy. J. Phys.:Conf. Ser. **700**, 012030 (2016). http://doi.org/10.1088/1742-6596/700/1/012030

3. T. Hassel, G. Klimov and A. Beniyash, Beam Extraction Using Non Vacuum Electron Beam by Reduced Acceleration Voltage. J. Phys.:Conf. Ser. **1109**, (2018). http://doi.org/10.1088/1742-6596/1109/1/012017

4. Z. Zhang and M. Zhang, Industrialization of Radiation-Induced Emulsion Polymerization ---- Technological Process and Its Advantages. Radiat. Phys. Chem., DOI: 10.1016/0969-806X(93)90229-N (1993). http://doi.org/10.1016/0969-806X(93)90229-N

5. R. O. Abdel Rahman and Y.-T. Hung, Application of Ionizing Radiation in Wastewater Treatment: An Overview. Water. **12**, (2019). http://doi.org/10.3390/w12010019

6. M. H. Casimiro, L. M. Ferreira, J. P. Leal et al., Ionizing Radiation for Preparation and Functionalization of Membranes and Their Biomedical and Environmental Applications. Membranes (Basel). **9**, (2019). http://doi.org/10.3390/membranes9120163

7. A. J. Berejka, M. R. Cleland and M. Walo, The Evolution of and Challenges for Industrial

Radiation Processing—2012. Radiation Physics and Chemistry. **94**, 141-146 (2014). http://doi.org/10.1016/j.radphyschem.2013.04.013

8.   K. Z. H. M. Dahlan, Application of Radiation Processing in Asia and the Pacific Region: Focus on Malaysia. Radiat. Phys. Chem. **46**, 1395-1400 (1995). http://doi.org/10.1016/0969-806X(95)00392-B

9.   S. Machi, New Trends of Radiation Processing Applications. Radiat. Phys. Chem. **47**, 333-336 (1996). http://doi.org/10.1016/0969-806X(95)00125-H

10.   B. Engin, C. Aydas and M. Polat, Detection of Gamma Irradiated Fig Seeds by Analysing Electron Spin Resonance. Food Chem. **126**, 1877-1882 (2011). http://doi.org/10.1016/j.foodchem.2010.12.012

11.   M.-A. Esnault, F. Legue and C. Chenal, Ionizing Radiation: Advances in Plant Response. Environmental and Experimental Botany. **68**, 231-237 (2010). http://doi.org/10.1016/j.envexpbot.2010.01.007

12.   S. M. Haji-Saeid, M. H. Sampa, A. Safrany et al., Radiation Processing Techniques in Remediation of Pollutants, and the Role of the Iaea in Supporting Capacity Building in Developing Countries. Radiation Physics and Chemistry. **81**, 1040-1044 (2012). http://doi.org/10.1016/j.radphyschem.2011.11.034

13.   J. Lilley and L. J. Murray, Radiotherapy: Technical Aspects. Medicine. **51**, 11-16 (2023). http://doi.org/10.1016/j.mpmed.2022.10.003

14.   J. Wang and J. Wang, Application of Radiation Technology to Sewage Sludge Processing: A Review. J. Hazard. Mater. **143**, 2-7 (2007). http://doi.org/10.1016/j.jhazmat.2007.01.027

15.   A. Waskow, D. Butscher, G. Oberbossel et al., Low-Energy Electron Beam Has Severe Impact on Seedling Development Compared to Cold Atmospheric Pressure Plasma. Sci. Rep. **11**, (2021). http://doi.org/10.1038/s41598-021-95767-0

16.   B. Xu and J. Wang, Radiation-Induced Modification of Chitosan and Applications for Water and Wastewater Treatment. Journal of Cleaner Production. **467**, (2024). http://doi.org/10.1016/j.jclepro.2024.142924

17.   M. N. Martins and T. F. Silva, Electron Accelerators: History, Applications, and Perspectives. Radiat. Phys. Chem. **95**, 78-85 (2014). http://doi.org/10.1016/j.radphyschem.2012.12.008

18.   J. Chen, M. Zhang, J. Shu et al., Electron Beam Irradiation-Induced Formation of Defect-Rich Zeolites under Ambient Condition within Minutes. Angew Chem Int Ed Engl. **60**, 14858-14863 (2021). http://doi.org/10.1002/anie.202103766

19.   M. Shi, T. Lin, Y. Wang et al., One-Step Radiation Synthesis of Novel Star-Shaped Polymeric Ionic Liquid–Poss Gel Electrolytes with High Ionic Conductivity and Mechanical Properties for Supercapacitor. Journal of Materials Science. **55**, 16347-16359 (2020). http://doi.org/10.1007/s10853-020-05162-9

20.   W. Zhao, J. Jiang, Y. Liu et al., Radiation Synthesis Strategy of Poly(Ionic Liquid)/Mxene Gel Polymer for Supercapacitor Electrolyte. Ionics. **29**, 2865-2875 (2023). http://doi.org/10.1007/s11581-023-05060-5

21.   X. Lv, B. Zhong, Y. Huang et al., Research Progress in Preparation and Application of Photonic Crystals. Chinese Journal of Mechanical Engineering. **36**, (2023). http://doi.org/10.1186/s10033-023-00836-2

22.   E. Damulira, M. N. S. Yusoff, A. F. Omar et al., A Review: Photonic Devices Used for Dosimetry in Medical Radiation. Sensors. **19**, (2019). http://doi.org/10.3390/s19102226

23.   Y. Fang, S. Y. Leo, Y. Ni et al., Optically Bistable Macroporous Photonic Crystals Enabled by Thermoresponsive Shape Memory Polymers. Adv. Opt. Mater. **3**, 1509-1516 (2015). http://doi.org/10.1002/adom.201500277

24.   J. Ge and Y. Yin, Responsive Photonic Crystals. Angew. Chem., Int. Ed. **50**, 1492-1522 (2011). http://doi.org/10.1002/anie.200907091

25.   J. Hou, H. Zhang, Q. Yang et al., Bio – Inspired Photonic – Crystal Microchip for Fluorescent Ultratrace Detection. Angew. Chem., Int. Ed. **53**, 5791-5795 (2014). http://doi.org/10.1002/anie.201400686

26.   Y. Wang, H. Cui, Q. Zhao et al., Chameleon-Inspired Structural-Color Actuators. Matter. **1**, 626-638 (2019). http://doi.org/10.1016/j.matt.2019.05.012

27.   Y. Wang, Q. Zhao and X. Du, Inkless Multi-Color Writing and Copying of Laser-Programmable Photonic Crystals. Materials Horizons. **7**, 1341-1347 (2020). http://doi.org/10.1039/d0mh00150c

28.   Y. Zhao, X. Zhao and Z. Gu, Photonic Crystals in Bioassays. Advanced Functional Materials. **20**, 2970-2988 (2010). http://doi.org/10.1002/adfm.201000098

29.   Z. Wang, X. Chen, T. Wang et al., A High-Resolution 3d Radiochromic Hydrogel Photonic Crystal Dosimeter for Clinical Radiotherapy. Mater Horiz. DOI: 10.1039/d4mh01235f, (2024). http://doi.org/10.1039/d4mh01235f

30.   Z. Wang, Y. Wang, Z. Ge et al., Color-Phase Readout Radiochromic Photonic Crystal Dosimeter. Matter. **5**, 4060-4075 (2022). http://doi.org/10.1016/j.matt.2022.08.015

31.   I. Janik, E. Kasprzak, A. Al-Zier et al., Radiation Crosslinking and Scission Parameters for Poly(Vinyl Methyl Ether) in Aqueous Solution. NUCL INSTRUM METH B. **208**, 374-379 (2003). http://doi.org/10.1016/s0168-583x(03)00897-8

32.   Zainuddin, J. Albinska, P. Ulański et al., Radiation-Induced Degradation and Crosslinking of Poly(Ethylene Oxide) in Solid State. J. Radioanal. Nucl. Chem. **253**, 339-344 (2002). http://doi.org/10.1023/A:1020406930244

33.   W. H. Eisa and Z. I. Ali, Characterization of Electron Beam Irradiated Poly Vinyl Alcohol/Poly Ethylene Glycol Blends. Journal of Scientific Research. **6**, 29-42 (2013). http://doi.org/10.3329/jsr.v6i1.13071

34.   C. P. Ennis and R. I. Kaiser, Mechanistic Studies on the Electron-Induced Degradation of Polymethylmethacrylate and Kapton. Phys. Chem. Chem. Phys. **12**, 14902-14915 (2010). http://doi.org/10.1039/c0cp01130d

35.   S. G. Abd Alla, H. M. Said and A. W. M. El – Naggar, Structural Properties of Γ – Irradiated Poly(Vinyl Alcohol)/Poly(Ethylene Glycol) Polymer Blends. Journal of Applied Polymer Science. **94**, 167-176 (2004). http://doi.org/10.1002/app.20842

36.   A. A. Alhazime, M. M. M. E. Barakat, K. Benthami et al., Gamma Irradiation – Induced Modifications in the Structural, Thermal, and Optical Properties of Polyvinyl Alcohol – Polyethylene Glycol/Cobalt Oxide Nanocomposite Films. Journal of Vinyl and Additive Technology. **27**, 347-355 (2020). http://doi.org/10.1002/vnl.21808

37.   S. D. Dipti Kakkar Thukral, Shelly Arora, Krishna Chuttani and Anil K Mishra, Potential Carriers of Chemotherapeutic Drugs: Matrix Based Nanoparticulate Polymeric Systems. Cancer Nanotechnol. **5**, 3 (2014). http://doi.org/10.1186/s12645-014-0003-9

38.   T. Sener Raman, M. Kuehnert, O. Daikos et al., A Study on the Material Properties of Novel Pegda/Gelatin Hybrid Hydrogels Polymerized by Electron Beam Irradiation. Front Chem. **10**,

1094981 (2022). http://doi.org/10.3389/fchem.2022.1094981

39. H. R. Ashjari, A. Ahmadi and M. S. S. Dorraji, Synthesis and Employment of Pegda for Fabrication of Superhydrophilic Pvdf/Pegda Electrospun Nanofibrous Membranes by in-Situ Visible Photopolymerization. Korean J. Chem. Eng. **35**, 289-297 (2017). http://doi.org/10.1007/s11814-017-0260-5

40. Y. H. C. C. Y. Chang, H. Li, C. Y. Chiu, Y. H. Yu, P. C. Chiang, Y. Ku, J. N. Chen, Kinetics of Decomposition of Polyethylene Glycol in Electroplating Solution by Ozonation with Uv Radiation. J. Environ. Eng. **127**, 908-915 (2001). http://doi.org/10.1061/(ASCE)0733-9372(2001)127:10(908)

41. J. O. Choi, J. A. Moore, J. C. Corelli et al., Degradation of Poly(Methylmethacrylate) by Deep Ultraviolet, X-Ray, Electron Beam, and Proton Beam Irradiations. J. Vac. Sci. Technol. B. **6**, 2286-2289 (1988). http://doi.org/10.1116/1.584071